RSC Advances

PAPER

View Article Online
View Journal | View Issue

Cite this: *RSC Adv.*, 2025, **15**, 13774

Synergistic experimental and computational investigation of azo-linked porphyrin-based porous organic polymers for CO_2 capture†

Barbara Panić, Tea Frey, Mladen Borovina, Petra Ištoković, Ivan Kodrin * and Ivana Biljan *

Received 15th November 2024
Accepted 1st April 2025

DOI: 10.1039/d4ra08113g

rsc.li/rsc-advances

We synthesized a series of azo-linked porphyrin-based porous organic polymers (APPs) with linear, bent, and trigonal linkers (**APP-1** to **APP-6**) and with directly connected tetraphenylporphyrin units (**APP-7a**, **APP-7b** and **APP-8**). The synthesized APPs are amorphous solids demonstrating good thermal stability and diverse BET surface areas. APPs with linkers showed significantly higher surface areas (469 to 608 $m^2\ g^{-1}$) compared to those with directly connected tetraphenylporphyrin units (0.3 to 23 $m^2\ g^{-1}$). Higher surface areas correlated with enhanced CO_2 adsorption, particularly for **APP-1**, **APP-2**, and **APP-5** with experimental CO_2 uptake values of 41 mg g^{-1}, 38 mg g^{-1}, and 38 mg g^{-1}, respectively, at 306 K. The computational study supported the experimental findings and provided insights on how surface area and the local landscape affect the CO_2 adsorption. Although the computational models were based on ideal structures, while the experiments revealed the materials were amorphous, the calculated CO_2 adsorption capacities were roughly comparable to the experimental results, particularly for the 3D systems (**APP-5** and **APP-6**) and the 2D systems with directly connected building units (**APP-7** and **APP-8**). Porphyrin units in the framework serve as additional binding sites for CO_2, especially when unhindered and available on either side of the porphyrin plane. This work highlights the potential of 2D layered APPs and 3D topologies for efficient CO_2 capture.

Introduction

Increased emissions of carbon dioxide (CO_2) into the atmosphere have been considered one of the major environmental issues in recent years due to their contribution to climate change.[1,2] The growing levels of atmospheric CO_2 are mainly caused by the combustion of fossil fuels for energy production. Despite rapid growth in renewable energy generation, CO_2 emissions from fossil fuels continued to rise in 2024.[3] In view of this, there is huge interest from scientists in developing advanced porous materials for CO_2 capture and separation. Among these, zeolites, activated carbons, metal organic frameworks (MOFs) and porous organic polymers (POPs) have received considerable attention as potential CO_2 adsorbents.[4–17] Although they exhibit high surface areas and exceptional CO_2 uptake capacities, the majority of these materials either lack chemical functionality (*e.g.*, activated carbons) or fail to maintain structural stability in the presence of water (*e.g.*, zeolites and MOFs).[12,18–20] POPs offer unique advantages due to their high chemical and physical stability, tunability and low density. The gas adsorption performance of POPs can be easily tailored by varying the monomer building units or introducing various functionalities in the porous networks.[21,22] Interactions between the POPs and CO_2 molecules can be improved by the incorporation of CO_2-philic nitrogen-rich moieties into the POP structure.[23–31] Patel *et al.* reported azo-bridged POPs, which exhibit excellent CO_2/N_2 selectivity with an increase in temperature making them ideal candidates for the post-combustion CO_2 capture.[27,29] These azo-linked POPs were synthesized by catalyst-free heterocoupling of aromatic nitro and amino monomers under basic conditions. Other common methods for the synthesis of azo-linked POPs include Zn- or $NaBH_4$-mediated reductive homocoupling of aromatic nitro monomers and copper(I)-catalyzed oxidative homocoupling of aromatic amino monomers.[32–35]

Owning to their exceptional photophysical and electrical properties, and rigid and tunable structure, porphyrins are frequently incorporated into various porous materials.[36–40] The presence of basic pyrrole segments that could facilitate interactions with CO_2 renders porphyrin-based POPs attractive potential CO_2 adsorbents.[36] Combining a porphyrin functional motif with CO_2-philic azo groups could lead to porous systems with enhanced CO_2 uptake capacity and selectivity. Indeed, reported azo-bridged porphyrin-based POPs exhibit remarkable CO_2 uptake capacities up to 3.98 mmol g^{-1} (at 273 K and 1 bar)

Department of Chemistry, Faculty of Science, University of Zagreb, Horvatovac 102a, Zagreb, HR-10000, Croatia. E-mail: ikodrin@chem.pmf.hr; ibiljan@chem.pmf.hr

† Electronic supplementary information (ESI) available. See DOI: https://doi.org/10.1039/d4ra08113g

and an excellent CO_2/N_2 selectivity up to 64.3 (at 273 K and 1 bar).[41–43] Furthermore, the CO_2/N_2 selectivity values showed an increase with increasing temperature, which makes the azo-bridged porphyrin-based POPs promising candidates for post-combustion CO_2 capture.[44] Recently, porphyrin-based azo POPs were also evaluated as catalysts for selective CO_2 capture and its conversion to cyclic carbonates.[45]

In our recent studies, we investigated, experimentally and computationally, structural and functional properties of POPs with different trigonal connectors (triphenylbenzene, triphenyltriazine, triphenylpyridine and triphenylamine) and various nitrogen–nitrogen linkages (azo, azoxy and azodioxy).[46–50] The results of the experimental part of those studies emphasized the influence of nitrogen–nitrogen linkages, building units and synthetic routes on the porosity and CO_2 adsorption capacities of the synthesized POPs, and identified several promising candidates for CO_2 adsorption.[47–50]

Computational studies facilitate not only the rationalization but also the prediction of the adsorption behaviour of POPs prior to their synthesis. By employing advanced modeling techniques like calculation of binding energies, electrostatic potential values (ESP) and grand-canonical Monte Carlo (GCMC) simulations, we can predict the binding affinities of POPs with CO_2, thereby optimizing the design for enhanced adsorption efficiency.[46–49] We suggested a simple model to estimate CO_2 uptake from the calculated ESP values[48] for different stacking modes of 2D layers with hexagonal pores and showed that the introduction of azodioxy in place of azo linkages can promote CO_2 binding. Even though this approach mainly relies on highly organized porous architectures, while actual systems are often amorphous, we found it very effective for the fast screening of targeted systems and achieved a nice agreement with experimental data. Pyridine-based azo-linked polymer TPP-azo exhibits CO_2 uptake of 32 mg g^{-1}, nicely matching the calculated values determined for configurations with displaced neighbouring layers (31 and 37 mg g^{-1}).[48]

Herein, we have extended our experimental and computational research on POPs to systems bearing tetragonal

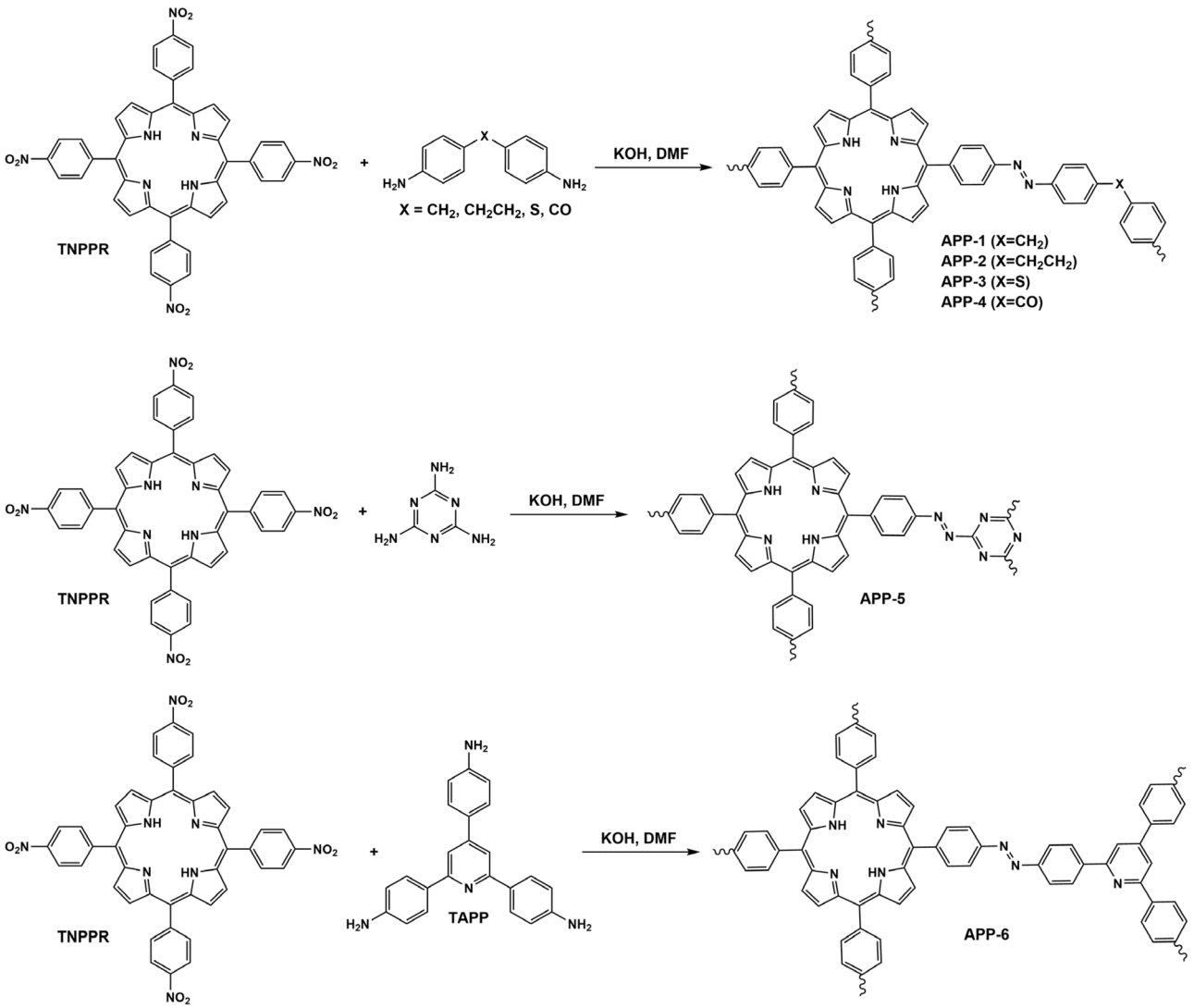

Fig. 1 Synthesis of APP-1 to APP-6 by heterocoupling of TNPPR and corresponding aromatic diamines and triamines.

tetraphenylporphyrin connector and azo linkages. It has previously been suggested that the introduction of flexible bridges between two phenyl rings (*e.g.*, ether links) in the aromatic diamino monomers used for the synthesis of porphyrin-based azo-linked POPs could induce enhanced porosity compared to *e.g.*, a rigid biphenyl linker.[44] To investigate more deeply the effect of flexible diamino linkers on the porosity and CO_2 adsorption capacity of azo-linked porphyrin-based POPs (APPs), herein, we synthesized polymers **APP-1** and **APP-2**, with the methylene and ethylene bridge, respectively, between the phenyl rings.

In addition, new porphyrin-based polymers incorporating semi-rigid sulphur (**APP-3**) and carbonyl bridge (**APP-4**) were prepared. Besides systems with diamino linkers, we also synthesized polymers **APP-5** and **APP-6** incorporating trigonal triamino linkers. Like porphyrin-based POPs known from the literature, **APP-1** to **APP-6** were synthesized by heterocoupling of 5,10,15,20-tetrakis(4-nitrophenyl)-21*H*,23*H*-porphyrin (**TNPPR**) and corresponding aromatic diamines and triamines (Fig. 1). In the present work, we also examined, for the first time to the best of our knowledge, oxidative homocoupling of 5,10,15,20-tetrakis(4-aminophenyl)-21*H*,23*H*-porphyrin (**TAPPR**) for the synthesis of **APP-7a** and reductive homocoupling of **TNPPR** and **TNPPR-Zn** for the synthesis of porphyrin-based polymers **APP-7b** and **APP-8**, respectively (Fig. 2). The structural and functional properties of synthesized polymers were thoroughly characterized by IR spectroscopy, ^{13}C CP/MAS NMR spectroscopy, powder X-ray diffraction (PXRD), elemental analysis, thermogravimetric analysis (TGA) and nitrogen (N_2) adsorption–desorption experiments. Furthermore, experimental data were augmented by computational study, employing periodic density functional theory (DFT) calculations and GCMC simulations.

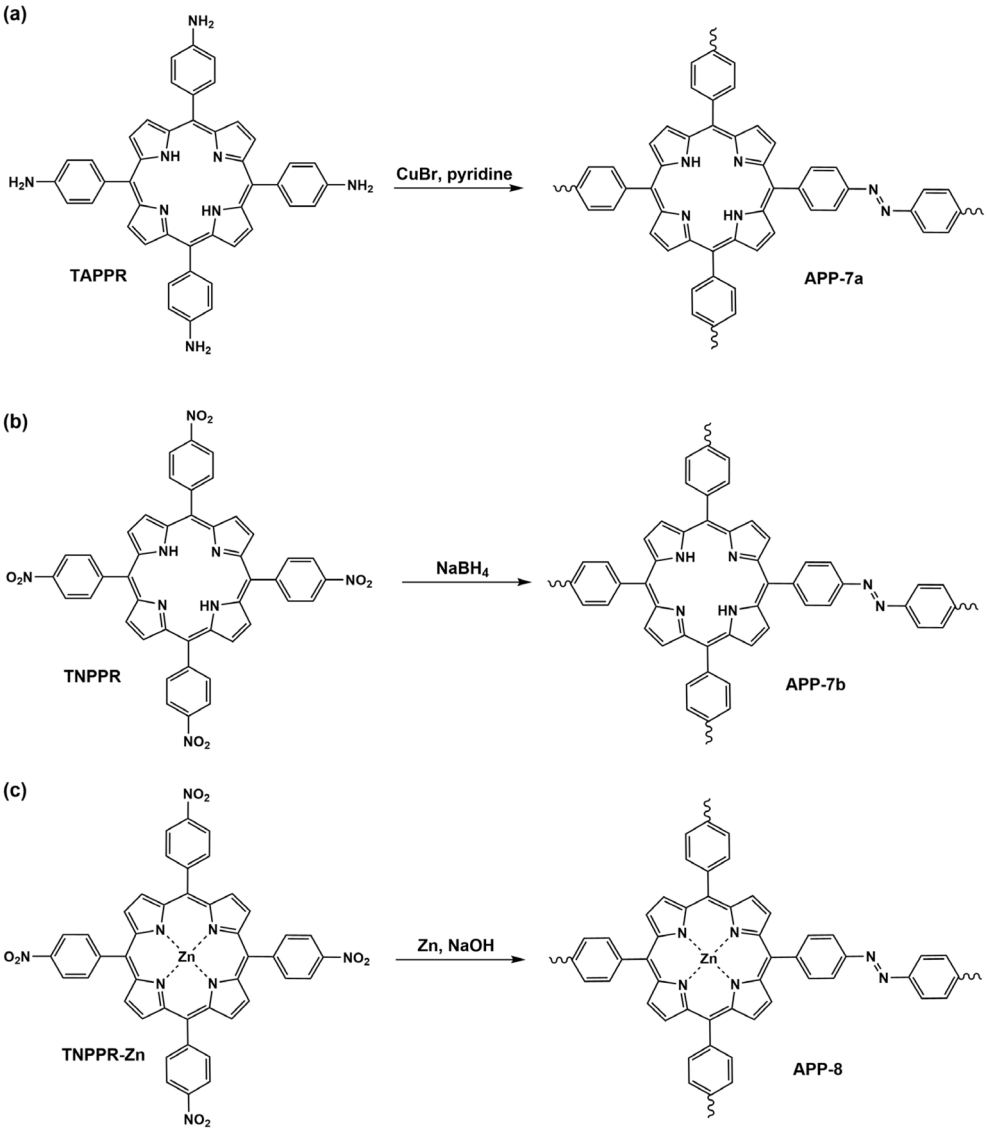

Fig. 2 Synthesis of APP-7a, APP-7b and APP-8 by homocoupling methods. (a) Cu(I)-catalysed oxidative homocoupling of TAPPR, (b) $NaBH_4$-mediated reductive homocoupling of TNPPR and (c) Zn-induced reductive homocoupling of TNPPR-Zn.

Results and discussion

Synthesis and characterization of APPs

APPs were synthesized using different synthetic methods by adopting the procedures reported in the literature.[27,29,32–35] For the synthesis of APPs incorporating diamino and triamino linkers, metal-catalyst free direct heterocoupling[27,29] of **TNPPR** and 4,4′-diaminodiphenylmethane (**APP-1**), 4,4′-ethylenedianiline (**APP-2**), 4,4-diaminodiphenyl sulphide (**APP-3**), 4,4′-diaminobenzophenone (**APP-4**), melamine (**APP-5**) and 2,4,6-tris(4-aminophenyl)pyridine (**TAPP**) (**APP-6**) were used (Fig. 1). APPs in which tetraphenylporphyrin units are directly connected by azo bonds were prepared *via* Cu(I)-catalysed oxidative homocoupling[34,35] of **TAPPR** (**APP-7a**) (Fig. 2a), $NaBH_4$-mediated reductive homocoupling[33] of **TNPPR** (**APP-7b**) (Fig. 2b), and Zn-induced reductive homocoupling[32] of **TNPPR-Zn** (**APP-8**) (Fig. 2c). All obtained APPs are insoluble in common organic solvents such as THF, DMF, DMSO, methanol, dichloromethane, chloroform and acetone, indicating the formation of cross-linked networks.

The presence of azo groups in APPs was confirmed by FTIR and ^{13}C CP/MAS NMR spectroscopy. The FTIR spectra of all APPs revealed the appearance of bands around 1470 and 1400 cm^{-1}, which can be attributed to the stretching vibrations of the azo (N=N) bonds (Fig. 3a–c and S5–S13†). The position of these bands is in good agreement with the stretching vibrations of azo bonds in similar azo-bridged porphyrin-based POPs, which appear at about 1470–1460 cm^{-1} and 1410–1400 cm^{-1}.[43–45,51] In addition, the asymmetric and symmetric stretching bands of unreacted nitro groups around 1510 and 1340 cm^{-1}, respectively, could be observed in the spectra of APPs. In the FTIR spectra of most APPs, the bands around 3400 and 3300 cm^{-1} assigned to the N–H stretching vibrations of unreacted amino groups were also detected. Nevertheless, the intensity of residual nitro and amino bands in APPs is attenuated when compared to starting nitro and amino monomers. The FTIR spectra of previously reported azo-linked porphyrin-based POPs also showed bands of attenuated intensity located at 1520–1510 cm^{-1} and 1350–1340 cm^{-1}, and 3500–3200 cm^{-1}, suggesting the presence of residual unreacted nitro and amino groups, respectively.[41,43–45,51] The successful formation of azo bridges was finally confirmed by the appearance of the characteristic signal of the carbon directly attached to the azo group (–C–N=N–) around δ = 150 ppm in the ^{13}C CP/MAS NMR spectra of all synthesized APPs (Fig. 4a–c and S22–S30†). The chemical shift of this signal is consistent with that of –C–N=N– carbons in other similar azo-linked POPs.[27,29,34,41,43,44,51] Furthermore, signals of carbon atoms of the porphyrin, phenyl and pyridine moieties, mostly situated at around 145, 130 and 118 ppm, were also observed in the ^{13}C CP/MAS NMR spectra of APPs and their chemical shifts are in good agreement with those of previously reported azo-linked POPs.[27,29,34,41,43,44,51] In addition, the ^{13}C CP/MAS NMR spectra of **APP-1** to **APP-6**, synthesized by heterocoupling of **TNPPR** and corresponding diamino and triamino linkers, and **APP-7a**, prepared by

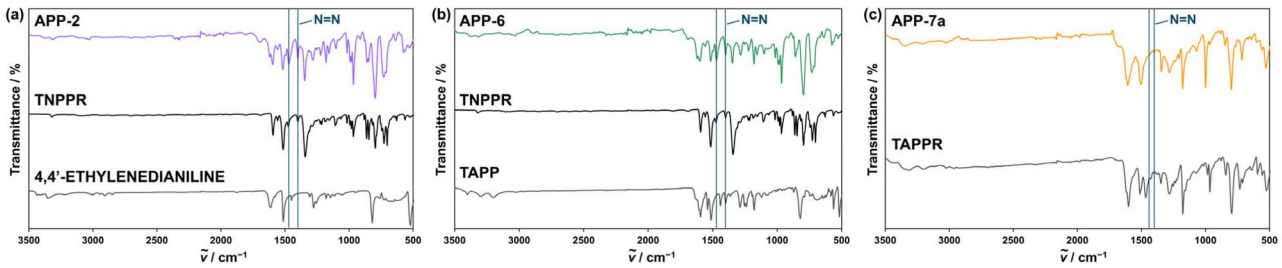

Fig. 3 Comparison of representative FTIR spectra of: (a) **APP-2** and starting nitro and amino monomers (**TNPPR** and 4,4′-ethylenedianiline, respectively), (b) **APP-6** and starting nitro and amino monomers (**TNPPR** and **TAPP**, respectively) and (c) **APP-7a** and starting amino monomer (). Signals attributed to the stretching vibrations of the azo (–N=N–) group in APPs are marked with vertical lines.

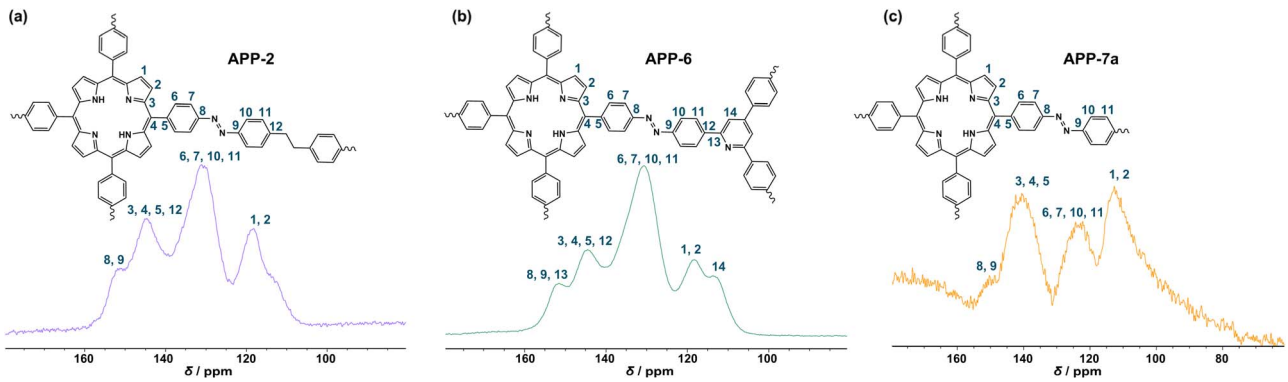

Fig. 4 Representative ^{13}C CP/MAS NMR spectra of: (a) **APP-2**, (b) **APP-6** and (c) **APP-7a**.

oxidative homocoupling of **TAPPR**, revealed signal around $\delta =$ 118 ppm, which is assigned to the carbon atom near amino group,[27] further indicating the presence of unreacted amino end groups.

The elemental analysis revealed some deviations between the experimentally determined and expected composition. Such discrepancies are frequently observed in POPs and can be attributed to incomplete polymerization and the presence of unreacted end groups, as well as adsorption of moisture and gases from air.[34,35,52–54]

PXRD pattern of all APPs showed broad diffraction peaks, indicating their amorphous nature (Fig. S31†). This is consistent with the previous reports on similar azo-bridged POPs, which are also amorphous due to the irreversible formation of azo bonds.[27,29,34,35,41–44,55,56]

The thermal stability of APPs was evaluated by TGA. The samples were heated up to 800 °C in N_2 atmosphere and held at isothermal conditions for 15 min at 800 °C. Samples **APP-1** (Fig. S32a and b†), **APP-2** (Figure S33a and b†), **APP-3** (Fig. S34a and b†), **APP-4** (Fig. S35a and b†), **APP-5** (Fig. S36a and b†) and **APP-6** (Fig. S37a and b†) display very similar thermal behaviour and show two decomposition events. They are all stable to around 250–270 °C when they slowly begin to decompose and exhibit ≤5.2% initial mass loss in a step that lasts until ∼430 °C when the rate of decomposition increases, and the second decomposition event starts where samples lose an additional 13.0–20.4% of their initial mass (depending on the sample) until approximately 620–640 °C. After that the rate slows down again and a trend of slow decomposition continues until 800 °C where it slows down again during the isothermal step. In all cases the first decomposition event shows slower decomposition rates than the second. Samples **APP-7a** (Fig. S38a and b†), **APP-7b** (Fig. S39a and b†), and **APP-8** (Fig. S40a and b†) start to decompose at a lower temperature of around 190–200 °C. Sample **APP-7a** shows similar thermal behaviour as samples **APP-1** to **APP-6** with a small decrease in mass (<3% of the initial mass) until ∼330 °C when the decomposition rate increases, however, the decomposition occurs in one continuous decomposition event which lasts until ∼650 °C during which the sample loses an additional 30.8% of its initial mass. After ∼670 °C another decomposition event starts and a small increase in the rate is observed which lasts until 800 °C when the rate gradually slows down during the isothermal step. Sample **APP-7b** shows two decomposition events below 650 °C, however, it is the only sample where the decomposition rate during the first event is higher than during the second event. It begins to slowly decompose (∼2% initial mass loss) until around 280 °C when the rate of decomposition increases, and the sample loses an additional 11% of its initial mass until ∼420 °C. The decomposition continues in the second event above 430 °C and the sample loses 10.4% of its initial mass until ∼640 °C. This sample also shows a third decomposition event starting at ∼720 °C where a small increase in the rate is observed which lasts until 800 °C when the rate decreases again during the isothermal step. The sample **APP-8** shows similar thermal behaviour as samples **APP-1** to **APP-6** with a slight difference in the first decomposition event. **APP-8** shows a higher decomposition rate starting at around 240 °C with another increase in the decomposition rate observed at 350 °C resulting in a loss of 6.8% of its initial mass until ∼420 °C. Around 430 °C the second decomposition event starts with an additional increase in the decomposition rate and a loss of 14% of its initial mass until ∼680 °C. The decomposition rate slows down and the slow decrease in mass continues until the end of the isothermal step at 800 °C.

Porosity features and CO_2 adsorption capacities of APPs

The porosity of APPs was studied by measuring N_2 adsorption–desorption isotherms at 77 K (Fig. 5a–c, S41a, S42a, S43a, S44a and S45a†). The surface areas were calculated by using the BET model and are listed in Table 1. The isotherms of **APP-1** to **APP-6** synthesized by heterocoupling of **TNPPR** and corresponding diamino and triamino linkers showed a high N_2 uptake at low relative pressures, followed by the gradual increase in N_2 uptake at higher relative pressures with the observed adsorption hysteresis (Fig. 5a, b, S41a, S42a, S43a and S44a†). These data suggested the presence of micropores and mesopores within the frameworks and were supported by the obtained pore size distributions (Fig. 5d, e, S41b, S42b, S43b and S44b†). The BET surface areas of **APP-1** to **APP-6** are in the range from 469 to 608 $m^2\ g^{-1}$. These values are comparable to the previously reported BET surface areas of similar azo-bridged porphyrin-based POPs prepared by the same synthetic method.[41–45] The BET surface areas of **APP-1** (598 $m^2\ g^{-1}$) and **APP-2** (594 $m^2\ g^{-1}$) bearing flexible methylene and ethylene bridge, respectively, between the phenyl rings are higher than that of the literature-known Azo-CPP-3 (514 $m^2\ g^{-1}$)[44] incorporating the rigid biphenyl linker. Furthermore, incorporation of flexible methylene and ethylene bridges in **APP-1** and **APP-2** further increased the porosity compared to the herein synthesized **APP-3** (586 $m^2\ g^{-1}$) and **APP-4** (469 $m^2\ g^{-1}$) with the semi-rigid sulphur and carbonyl bridge, respectively, and previously reported Azo-CPP-5 (563 $m^2\ g^{-1}$)[44] with the semi-rigid oxygen bridge. As suggested earlier, although the flexibility leads to increased conformational freedom and consequently more efficient space filling in the network, it also eliminates the constraint of in-plane alignment of the biphenyl azo moieties.[27,44] Surprisingly, much lower values of BET surface areas were obtained for **APP-7a**, **APP-7b** and **APP-8**, in which tetraphenylporphyrin units are directly connected *via* azo bonds. According to the pore size distribution, these polymers mostly contain mesopores and macropores (Fig. 5f and S45b†). **APP-7a**, synthesized by Cu(I)-catalysed oxidative homocoupling of **TAPPR**, showed a somewhat higher BET surface area (23 $m^2\ g^{-1}$) compared to the **APP-7b** (0.3 $m^2\ g^{-1}$), which is composed of the same building units but synthesized by $NaBH_4$-mediated reductive homocoupling of **TNPPR**. We also tried the reductive homocoupling of **TNPPR** with Zn as a reducing reagent. However, the reaction was not successful. Therefore, we synthesized Zn(II) derivative of **TNPPR** (**TNPPR-Zn**), which was then subjected to the Zn-mediated reductive homocoupling. Although this reaction afforded the targeted azo-linked polymeric product **APP-8**, the introduction of Zn into the porphyrin ring and the change in the reducing

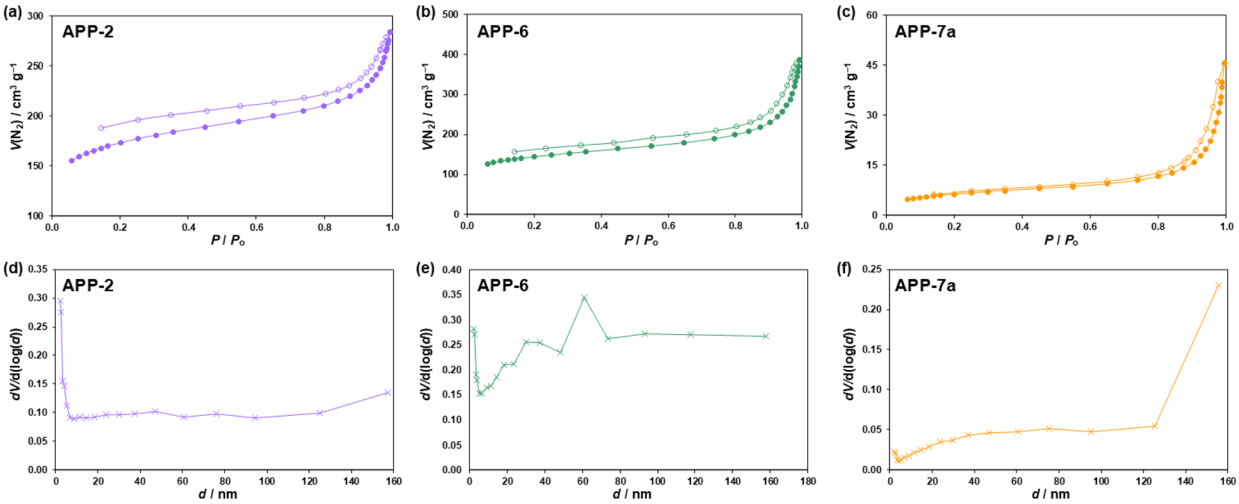

Fig. 5 Representative N_2 adsorption–desorption isotherms of: (a) **APP-2**, (b) **APP-6** and (c) **APP-7a** measured at 77 K. The adsorption and desorption isotherms are depicted with filled and open markers, respectively. Pore size distributions of: (d) **APP-2**, (e) **APP-6** and (f) **APP-7a**.

Table 1 Experimental and calculated surface areas and CO_2 uptakes of APPs

	Experimental		Calculated	
Compound	BET surface area ($m^2\ g^{-1}$)	CO_2 uptake[b] (mg g^{-1})	Average surface area ($m^2 g^{-1}$)	CO_2 uptake[c] (mg g^{-1})
APP-1	598	41	1969	13
APP-2	594	38	2246	18
APP-3	586	29	1931	15
APP-4	469	30	1934	20
APP-5	608	38	6777	49
APP-6	500	28	7567	49
APP-7a[a]	23	15	1332	23
APP-7b[a]	0.3	22	1332	23
APP-8	3	28	1195	21

[a] Different synthetic methods. Labeled as **APP-7** in the computational study. [b] At approximately 306 K. [c] At a pressure of 1 bar and 298 K.

reagent did not result in a significant increase in porosity compared to **APP-7b**.

The CO_2 adsorption capacities of APPs were investigated by thermogravimetric analysis at approximately 306 K and the data are summarized in Table 1. All measured samples have shown an increase in mass when switching to CO_2 atmosphere and a decrease in mass when switching back to N_2 atmosphere (Fig. 6a–c and S32c–S40c†). The transition for most samples was sharp (plateau and baseline values reached relatively quickly upon change of atmosphere) and their mass decreased back to baseline values during N_2 atmosphere cycles. Samples **APP-7a** (Fig. 6c) and **APP-7b** (Fig. S39c†) exhibit distinct behaviour. While most of the mass increase occurred during the first 5 minutes of the CO_2 atmosphere cycles, both samples show a gradual increase in mass and **APP-7a** reaches a plateau after approximately 12 minutes while **APP-7b** continues to slowly increase in mass during the whole CO_2 cycle. These samples also show different CO_2 desorption behaviour. While most of the reduction in mass occurs during the first 5 minutes of the N_2 cycles the process gradually slows down and baseline values were not reached even after 20 minutes of the N_2 cycles. Some of the major factors influencing the CO_2 uptake capacity of POPs include their surface area, pore structure and incorporation of heteroatoms in the building units.[28] In general, the higher BET surface areas of **APP-1** to **APP-6**, which incorporate various diamino or triamino linkers, led to higher CO_2 uptake values compared to **APP-7a**, **APP-7b** and **APP-8** in which tetraphenylporphyrin units are directly connected *via* azo linkages and which show much lower BET surface areas. The highest CO_2 adsorption capacities were observed for **APP-1** (41 mg g^{-1}) and **APP-2** (38 mg g^{-1}) containing flexible methylene and ethylene bridge, respectively, and **APP-5** (38 mg g^{-1}) bearing nitrogen-rich melamine linker. These APPs also showed the highest BET surface areas. Nevertheless, as suggested previously, a high value of BET surface area is not necessarily a determining factor for CO_2 adsorption affinity, and POPs with BET surface areas lower than 100 $m^2\ g^{-1}$ can show good CO_2 uptake capacities.[27,28,57] This is nicely corroborated from the CO_2 adsorption capacities obtained for **APP-7a** (15 mg g^{-1}), **APP-7b** (22 mg g^{-1}) and **APP-8** (28 mg g^{-1}) which all display low BET surface areas, indicating that the presence of CO_2-philic azo groups and pyrrole rings contributes most to CO_2 binding affinity of these

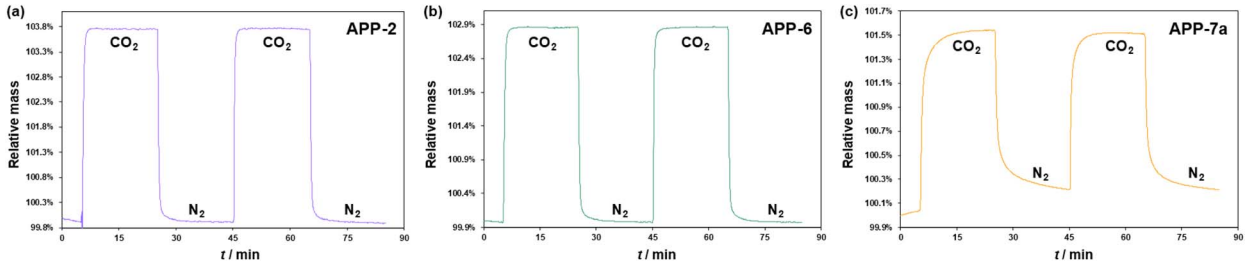

Fig. 6 Representative thermogravimetric CO_2 adsorption and desorption profiles of (a) **APP-2**, (b) **APP-6** and (c) **APP-7a** at approximately 306 K.

three APPs. The introduction of Zn to the inner core of the porphyrin ring in **APP-8** proves to be beneficial for the increase in CO_2 uptake capacity compared to the free base porphyrin polymers **APP-7a** and **APP-7b**. Noteworthy, the CO_2 uptake capacity of **APP-8** of 28 mg g^{-1} is comparable to the CO_2 uptake values of some APPs with diamino (*e.g.*, **APP-3** and **APP-4**) and triamino (*e.g.*, **APP-6**) linkers, although the BET surface area of **APP-8** is much lower. The CO_2 uptake capacities of APPs are comparable to some reported azo-linked porphyrin-based POPs such as Azo-CPP-1 (48 mg g^{-1} at 303 K), Azo-CPP-3 (39.9 mg g^{-1} at 303 K), Azo-CPP-6 (40.2 mg g^{-1} at 303 K) and Azo-CPP-7 (41.7 mg g^{-1} at 303 K).[44] In addition, these values are comparable or higher than those of other azo-linked POPs *e.g.*, azo-COPs (15–31 mg g^{-1} at 323 K) built from 3D tetrahedral building units,[29] and pyridine-based TPP-azo (32 mg g^{-1} at 303 K),[48] but lower than those of *e.g.*, benzene-based azo-linked ALP-4 (81 mg g^{-1} at 298 K).[34]

Computational study. We employed a computational study to get additional insight into the structural and CO_2 adsorption properties of the synthesized APPs. First, we optimized six azo systems comprising directly linked tetraphenylporphyrin-based units (**APP-7** and **APP-8**) and those bridged by linear (**APP-2**) and bent linkers (**APP-1**, **APP-3**, and **APP-4**). These systems consist of 2D layers that are ordered in AA fashion along the third dimension. The major difference between the investigated systems is in the distinct shapes and dimensions of their 2D pores. Directly linked tetraphenylporphyrin connectors (**APP-7** and **APP-8**) and those bridged by the linear –Ph–CH_2–CH_2–Ph– linkers (**APP-2**) induce the formation of nearly perfect rhombohedral pores (Fig. 7b and c), whereas the bent –Ph–CH_2–Ph– (**APP-1**), –Ph–S–Ph– (**APP-3**), and –Ph–CO–Ph– linkers (**APP-4**) form distorted rectangular-like pores (Fig. 7a). In contrast, compounds **APP-5** and **APP-6** built from tetragonal-like and trigonal building units form real 3D azo-linked systems (Fig. 7d).

Although, depending on their conformational flexibility, tri- and tetratopic linkers can acquire 2D nets[58–60] and various 3D topologies,[61] in this paper, we have focused only on topologies commonly referred to as pto topologies.[62] Such systems are characterized by low densities and high porosity when compared to other crystalline framework materials.[62]

The discrepancy between the calculated average surface areas and the experimentally determined values can be attributed to the methodology employed in the computational study. We assumed highly ordered AA structures with perfectly aligned neighbouring layers, as AA eclipsed stacking typically exhibits the lowest energies compared to AB staggered, inclined and serrated configurations.[48] However, such highly ordered structures were not achievable experimentally. PXRD experiments indicated the amorphous nature of all investigated APPs, which is reflected in significantly lower BET surface areas.

Overall, systems exhibiting the highest average surface areas, such as **APP-5** and **APP-6** with pto topologies, also show the greatest available pore volumes, subsequently leading to an enhanced capacity for CO_2 adsorption of 49 mg g^{-1} (Fig. 7e, Table 1 and S7†). The calculated CO_2 uptake values are very similar in other APPs with AA stacked layers. Slightly increased CO_2 uptakes of 23 and 21 mg g^{-1} are observed for APPs with directly connected porphyrin rings and rhombohedral pores, **APP-7** and **APP-8**, respectively. In comparison, slightly lower CO_2 uptakes of 13 and 15 mg g^{-1} are found in 2D systems with rectangular-like pores, **APP-1** and **APP-3**, respectively. This indicates that not only the topology and dimensionality of the system (3D *vs.* 2D) but also pore dimensions and shapes can influence the framework's ability to bind CO_2.

While a direct correspondence between calculated and experimental values is not always observed, **APP-5**, which has the highest surface area, also exhibits one of the highest CO_2 uptakes both, experimentally (38 mg g^{-1}) and computationally (49 mg g^{-1}). The experimental and calculated CO_2 uptakes are quite similar for the systems with directly connected porphyrin units, such as **APP-7** (22 *vs.* 23 mg g^{-1}) and **APP-8** (28 *vs.* 21 mg g^{-1}). This observation aligns with our previous findings for directly attached trigonal building units,[47,48] which partly justified the approach of assuming AA stacking of neighbouring layers. Interestingly, the experimentally observed higher CO_2 binding in amorphous APPs with bridged porphyrin units (**APP-1** to **APP-4**) compared to **APP-7** and **APP-8**, which have directly connected porphyrins, shows an opposite trend to their calculated AA analogues.

To further investigate this discrepancy, we generated density plots revealing the spatial distribution of CO_2 molecules (Fig. 8a, b and S59†). Regions of high adsorption density are positioned along the pore walls of AA stacked APPs, specifically near the azo linkages and the outer parts of porphyrin rings. Additionally, 3D **APP-5** and **APP-6** indicated areas above and below the porphyrin rings as highly probable binding sites for CO_2 molecules.

Besides the surface area available for CO_2 adsorption, the local landscape of the surface, with binding sites of varying

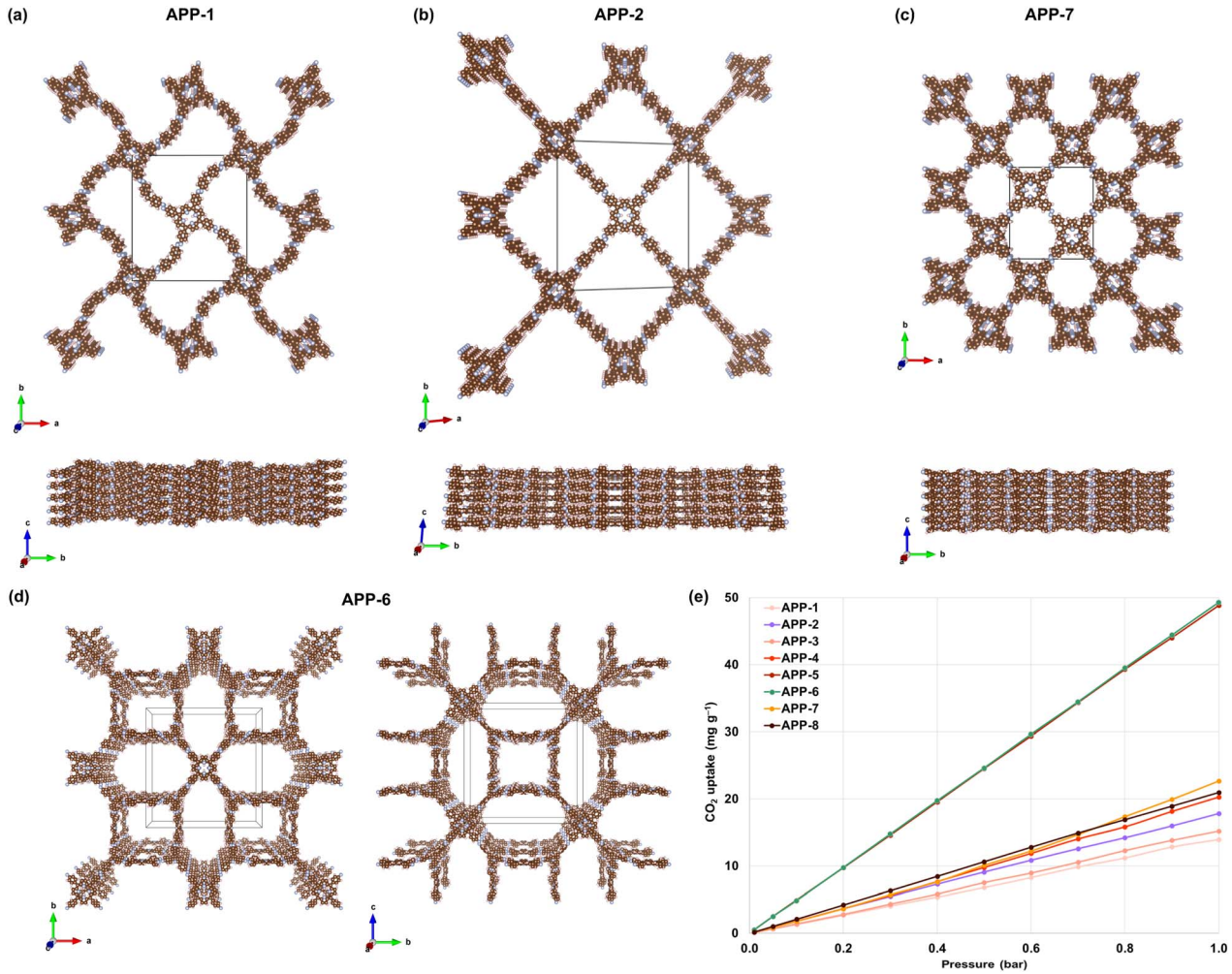

Fig. 7 Optimized geometries (PBE-D3/pob-TZVP-rev2) of: (a) 2D-layered **APP-1**, (b) 2D-layered **APP-2**, (c) 2D-layered **APP-7** and (d) 3D **APP-6**. Views along the crystallographic *a* and *c* axes. (e) CO_2 adsorption isotherms of modeled APPs at 298 K.

shapes and electrostatic potential values (ESP), can also affect the strength of different CO_2 binding modes onto the framework's surface. The density plots align well with the calculated ESP maps (Fig. 8a, b and S60†), showing that areas with the most positive or negative ESP values match the spatial distribution of CO_2 molecules. The impact of APPs dimensionality on CO_2 adsorption is clearly demonstrated by comparing the AA stacked 2D configurations with the 3D networks of **APP-5** and **APP-6**. In all APPs, the inner parts of porphyrin rings display significant negative ESP values, suggesting potential interactions with CO_2 molecules. However, such interactions are only achieved if the inner parts of the porphyrin rings have surface area available for binding gas molecules, as seen in the 3D **APP-5** and **APP-6**.

To explore this hypothesis further, we selected **APP-2** with linearly bridged porphyrin rings to compare its structural and adsorption properties. This comparison focuses on the effects of neighbouring layer slippage, which opens the inner regions of the porphyrin rings to interact with CO_2 molecules. The computational analysis was extended to two limiting cases: the AA (eclipsed) configuration, showing perfectly aligned layers, and the AB (staggered) configuration, with maximally displaced neighbouring layers (Fig. 8c). Although both systems, **APP-2$_{AB}$** and **APP-2$_{AA}$**, have very similar average surface areas (2388 and 2246 m^2g^{-1}, respectively), the unhindered porphyrin ring creates additional binding sites for interaction with CO_2 molecules, as confirmed by density plot of **APP-2$_{AB}$** (Fig. 8b). This type of structural modification significantly increased the calculated CO_2 uptake from 18 to 238 mg g^{-1} and changed the CO_2/N_2 selectivity from 4.4 to 21.4. However, **APP-2$_{AB}$** is 100.5 kJ mol^{-1} less stable than its **APP-2$_{AA}$** analogue, making it an unlikely configuration to be acquired. As experimentally determined APPs were found to be amorphous, without well-ordered structure, they can potentially have unhindered porphyrin positions. Despite having relatively smaller average surface areas compared to the calculated values of perfectly ordered AA compounds, these amorphous structures can exhibit different CO_2 uptake values due to the porphyrin rings being free to interact with CO_2 molecules. Nevertheless, the agreement between the 3D (*e.g.*, **APP-5** and **APP-6**) and 2D AA configurations of directly connected building units (*e.g.*, **APP-7**

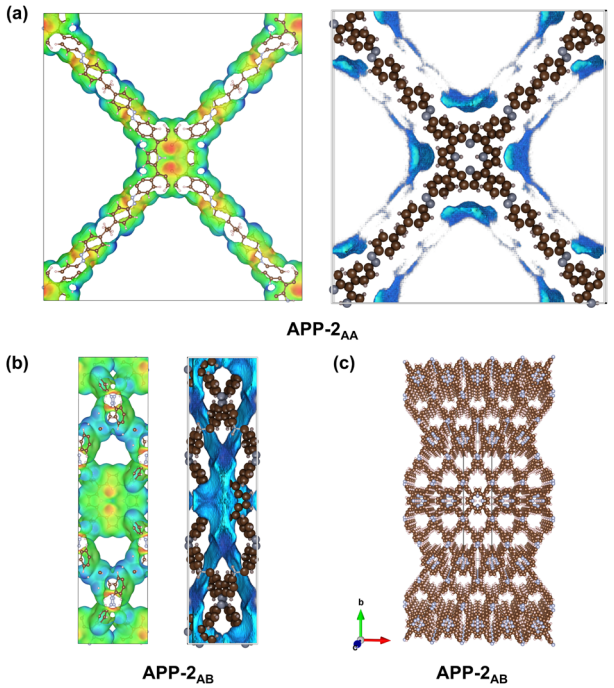

Fig. 8 Electrostatic potential maps (left panel) and density plots (right panel) showing the average CO_2 distribution at 298 K and 1 bar for AA stacking (a) and AB stacking (b) modes of **APP-2**. Optimized geometry (PBE-D3/pob-TZVP-rev2) of AB stacked **APP-2** (c).

and **APP-8**) is quite good for a preliminary estimate of their CO_2 adsorption potential.

Experimental

Synthesis and general information

All chemicals were used as received from suppliers. **APP-1** to **APP-8** were synthesized using different synthetic methods by adopting the procedures reported in the literature.[27,29,32–35] 5,10,15,20-tetrakis(4-nitrophenyl)-21*H*,23*H*-porphyrin (**TNPPR**), 5,10,15,20-tetrakis(4-nitrophenyl)-21*H*,23*H*-porphyrin-Zn(II) (**TNPPR-Zn**), 5,10,15,20-tetrakis(4-aminophenyl)-21*H*,23*H*-porphyrin (**TAPPR**) and 2,4,6-tris(4-aminophenyl)pyridine (**TAPP**) were synthesized by the modified procedures described in the literature.[63–65] Other aromatic amines were purchased from the suppliers. The details of the synthetic procedures and products data are provided in the ESI.†

The synthesized compounds were identified by solution ^1H and ^{13}C NMR spectroscopy, solid-state ^{13}C CP/MAS NMR spectroscopy, IR spectroscopy, PXRD and elemental analysis. Solution-state ^1H and ^{13}C NMR spectra were recorded on a Bruker Ascend 400 MHz NMR spectrometer at 25 °C. DMSO-d_6 was used as a solvent and TMS as an internal standard for chemical shifts. Solid-state ^{13}C CP/MAS NMR spectra were recorded on a Bruker Avance Neo 400 MHz NMR spectrometer and Bruker Avance III HD 400 MHz NMR spectrometer at spinning rates of 10 and 15 kHz, respectively. FTIR spectra were recorded on a PerkinElmer UATR two spectrometer in the spectral range between 4000 cm^{-1} and 400 cm^{-1} at a resolution of 4 cm^{-1}, averaging 10 scans per spectrum. Elemental analysis was provided by the Analytical Services Laboratory of the Ruđer Bošković Institute, Zagreb, Croatia. PXRD diffractograms were recorded on a Malvern Panalytical Aeris powder diffractometer in Bragg–Brentano geometry with PIXcel1D detector. Thermogravimetric analysis was carried out using a simultaneous TGA-DTA analyzer Mettler-Toledo TGA/DSC 3+. Samples were placed in alumina pans (70 μL) and heated in flowing nitrogen (50 mL min^{-1}) from 30 °C up to 180 °C at a rate of 10 °C min^{-1} and held in isothermal conditions for 10 minutes at 180 °C to remove traces of solvents. Afterwards, samples were cooled to room temperature and heated in flowing nitrogen (50 mL min^{-1}) from 25 °C up to 800 °C at a rate of 10 °C min^{-1} and held in isothermal conditions for 15 minutes at 800 °C. CO_2 sorption experiments were carried out by following a previously reported procedure with minor modifications in experimental conditions.[66] Before performing CO_2 adsorption experiments, a 70 μL alumina pan was filled with a fresh sample, heated to 100 °C at a heating rate of 20 °C min^{-1} in nitrogen atmosphere (flow rate 150 mL min^{-1}) and held at 100 °C for 30 minutes to dry the sample. After drying, CO_2 adsorption was measured by switching between N_2 atmosphere and CO_2 atmosphere in 20 min intervals (flow rates for both gases were 150 mL min^{-1}) at ~30 °C. The measured sample temperature varied around 33 °C during CO_2 cycles. To correct for different buoyancy effects on the TG scale and alumina pan, a baseline curve was recorded under the same experimental conditions using an empty alumina pan and subtracted from the measured curve. Data collection and analysis were performed using the program package STARe Software 16.40 MettlerToledo GmbH. The specific surface area was determined from N_2 gas adsorption–desorption data obtained with Micromeritics ASAP-2000 at 77 K. Before analysis, samples were degassed at 150 °C under a dynamic vacuum of 7 mPa. The adsorption data were used to calculate the surface area with the BET model, using data points within the linear region of the BET isotherm ($P/P_0 = 0.05–0.3$). The pore size distribution was determined using the Barrett–Joyner–Halenda (BJH) method.

Computational details

The initial geometries of APPs were generated based on previously reported azodioxy-linked[67] and imine-linked[68] porphyrin COFs. First, structural effects were analysed on the simple model compound with directly attached porphyrin rings, **APP-7**. Conformational preferences for the relative orientation of phenyl substituents and azo bonds were analysed in 0D, 2D, and 3D systems of **APP-7**. More details are available in the ESI.†. The most stable conformation was selected for further modification and generation of compounds **APP-1** to **APP-4**, **APP-8**. These compounds geometries were first generated as 2D layers that were converted into 3D crystal structures after optimization with the same principles as **APP-7**. The initial geometries of **APP-5** and **APP-6** were generated based on previously reported 3D pto COF topology constructed from square-planar and trigonal-planar building units.[62] The space group symmetry of all crystal structures was determined and confirmed with PLATON.[69] All structures were visualized using VESTA program.[70]

Periodic density functional theory (DFT) calculations were performed in CRYSTAL17 (ref. 71) using the PBE functional[72] with Grimme's D3 correction for a better description of the weak dispersive interactions.[73] Triple-zeta basis set pob-TZVP-rev2, adapted for periodic calculations, was employed for all atoms.[74] The input files for CRYSTAL17 were created from cif files with cif2cell package.[75] Full optimization of both atom coordinates and unit cell parameters were performed with default convergence criteria. Total energy convergence was set to 10^{-7} and truncation criteria for the calculations of coulombs and exchange integrals increased to (8 8 8 8 16) for SCF calculations. The reciprocal space was sampled using $2 \times 2 \times 8$ Pack–Monkhorst *k*-point mesh for **APP-1** to **APP-4**, **APP-7**, **APP-8** while $2 \times 2 \times 2$ Pack–Monkhorst *k*-point mesh was used for **APP-5** and **APP-6**. The same level of theory and optimization criteria were used on 2D layers (keyword SLAB for 2D system in CRYSTAL 17) and 3D crystal structures. The lattice parameters and other relevant data of the DFT-optimized structures are given in the ESM.†

The net atomic charges were calculated using the REPEAT method[76] from electrostatic potential values calculated by CRYSTAL17. Accessible surface areas of all compounds were calculated by Monte Carlo sampling approach with a spherical probe of the 1.55 Å (nitrogen Wan der Vaals radius) using Zeo++ code.[77] The grand canonical Monte Carlo (GCMC) simulation was performed to obtain the single component adsorption isotherms of CO_2 at 298 K using RASPA code.[78] For the modeling of the interactions between gas molecules and framework, the site–site Lennard-Jones (LJ) potential and coulombic interactions were used together with Lorentz–Berthelot mixing rules for the LJ interactions between different atoms. A three-site model was used to describe the CO_2 gas molecules within the TraPPE force field.[79] Other atoms from the framework were modeled using the DREIDING force field.[80] Default cut-off value, as suggested by the RASPA code, was used for LJ and the short-range part of the coulombic interactions. The long–range interactions were evaluated by the Ewald summation method with a default relative precision of 10^{-6}. The pressure was converted to fugacity using the Peng–Robinson equation of state and further used to calculate the chemical potential. In total $2 \times 2 \times 8$ unit cells were used to obtain a valid GCMC simulation cell with a requirement that all the perpendicular cell lengths have to be larger than twice the default cut-off distance of 12 Å. During the optimisation, framework atoms were frozen. Four different MC moves of gas molecules (translation, rotation, reinsertion, and swap) were allowed during the simulation. More than 10^6 cycles were used for the equilibration and production phases. The heats of adsorption were also calculated based on the RASPA code, from the limit of using a single adsorbate under zero loading by assuming the framework is rigid. Pore shapes and density pictures for the adsorption of CO_2 at 298 K and 1.0 bar were obtained as described in the RASPA manual. Density plots illustrating CO_2 binding at 298 K and 1.0 bar were generated using the procedure outlined in the RASPA code and subsequently visualized with the Visualization Toolkit (VTK). The electrostatic potential values are mapped onto the 0.002 a.u. isodensity surface. Additional details can be found in the ESI.†

Conclusions

A series of azo-linked porphyrin-based porous organic polymers (APPs) bearing linear, bent and trigonal linkers between the tetraphenylporphyrin units (**APP-1** to **APP-6**) were synthesized by heterocoupling of **TNPPR** and various aromatic diamines and triamines. In addition, for the first time to the best of our knowledge, APPs in which tetraphenylporphyrin units are directly connected *via* azo bonds were prepared by oxidative homocoupling of **TAPPR** (**APP-7a**), and reductive homocoupling of **TNPPR** (**APP-7b**) and **TNPPR-Zn** (**APP-8**). While the synthesized materials are all amorphous solids of good thermal stability, they exhibit various BET surface areas. In general, **APP-1** to **APP-6** incorporating linkers between the tetraphenylporphyrin moieties show much higher BET surface areas (from 469 to 608 $m^2\ g^{-1}$) compared to the **APP-7a** (23 $m^2\ g^{-1}$), **APP-7b** (0.3 $m^2\ g^{-1}$) and **APP-8** (3 $m^2\ g^{-1}$) in which tetraphenylporphyrin units are directly linked *via* azo bonds. The obtained results indicate the pronounced influence of synthesis method and building units on the porosity of the final APPs. Furthermore, APPs with good BET surface areas also show the enhanced CO_2 adsorption capacities with the highest values observed for **APP-1** (41 mg g^{-1}) and **APP-2** (38 mg g^{-1}) with flexible methylene and ethylene bridge, respectively, and **APP-5** (38 mg g^{-1}) containing nitrogen-rich melamine linker. However, the differences in CO_2 uptake capacities of APPs with (**APP-1** to **APP-6**) and without (**APP-7a**, **APP-7b** and **APP-8**) linkers between tetraphenlyporphyrin units are less obvious compared to variations in their BET surface areas. These findings suggest that favourable interactions between CO_2-philic azo groups and pyrrole rings contribute significantly to the CO_2 binding affinity of APPs.

The computational study supported the experimental findings and provided additional insights into the structural characteristics influencing CO_2 uptake. Despite the computational models being based on ideal structures while the experiments revealed the materials were amorphous, the calculated CO_2 adsorption capacities were roughly comparable to the experimental results, particularly for the 3D systems (*e.g.*, **APP-5** and **APP-6**) and the 2D systems with directly connected building units (*e.g.*, **APP-7** and **APP-8**). Density plots and electrostatic potential maps highlighted the importance of available surface areas and their local landscape on CO_2 adsorption. The porphyrin building units introduced into the framework act as additional binding sites for CO_2 molecules, especially when the units are unhindered and available to bind CO_2 molecules on either side of the porphyrin plane.

Finally, this work represents the successful construction of APPs through the rational design of carefully selected connectors and linkers. The experimental study indicated that 2D APP analogues with linkers and 3D topologies may enhance CO_2 adsorption performance compared to directly attached tetraphenylporphyrin units. This advancement highlights the potential applications of APPs as efficient CO_2 adsorbents.

Data availability

The data supporting this article have been included as part of the ESI.†

Author contributions

Conceptualisation, I. K. and I. B.; methodology, M. B., I. K. and I. B.; software, I. K.; validation, B. P., T. F, I. K. and I. B.; investigation, B. P., T. F., M. B., P. I., I. K. and I. B.; writing – original draft preparation, B. P., T. F., M. B., I. K. and I. B.; writing – review and editing, I. K. and I. B.; visualisation, B. P., T. F., M. B., I. K. and I. B.; supervision, I. K. and I. B.; project administration, I. K. and I. B.; funding acquisition, I. B. All authors have given approval to the final version of the manuscript.

Conflicts of interest

There are no conflicts to declare.

Acknowledgements

This work has been fully supported by Croatian Science Foundation under the project IP-2020-02-4467. The support of project CIuK (Grant KK.01.1.1.02.0016) co-financed by the Croatian Government and the European Union through the European Regional Development Fund – Competitiveness and Cohesion Operational Program is acknowledged. We thank Prof Gordana Matijašić (University of Zagreb, Croatia) for nitrogen adsorption–desorption measurements and assistance with the data interpretation.

Notes and references

1 K. O. Yoro and M. O. Daramola, in *Advances in Carbon Capture*, Elsevier, 2020, pp. 3–28.
2 L. J. R. Nunes, *Environments*, 2023, **10**, 66.
3 *Global Fossil CO_2 Emissions Are Projected to Continue to Rise in 2024*, **https://www.cicero.oslo.no/en/articles/global-fossil-co-emissions-are-projected-to-continue-to-rise-in-2024**, accessed 24 October 2024.
4 M. Sai Bhargava Reddy, D. Ponnamma, K. K. Sadasivuni, B. Kumar and A. M. Abdullah, *RSC Adv.*, 2021, **11**, 12658–12681.
5 S. Kumar, R. Srivastava and J. Koh, *J. CO_2 Util.*, 2020, **41**, 101251.
6 D. G. Boer, J. Langerak and P. P. Pescarmona, *ACS Appl. Energy Mater.*, 2023, **6**, 2634–2656.
7 S. Acevedo, L. Giraldo and J. C. Moreno-Piraján, *ACS Omega*, 2020, **5**, 10423–10432.
8 G. Singh, J. Lee, A. Karakoti, R. Bahadur, J. Yi, D. Zhao, K. AlBahily and A. Vinu, *Chem. Soc. Rev.*, 2020, **49**, 4360–4404.
9 Z. Li, P. Liu, C. Ou and X. Dong, *ACS Sustainable Chem. Eng.*, 2020, **8**, 15378–15404.
10 T. Ghanbari, F. Abnisa and W. M. A. Wan Daud, *Sci. Total Environ.*, 2020, **707**, 135090.
11 C. A. Trickett, A. Helal, B. A. Al-Maythalony, Z. H. Yamani, K. E. Cordova and O. M. Yaghi, *Nat. Rev. Mater.*, 2017, **2**, 17045.
12 K. Sumida, D. L. Rogow, J. A. Mason, T. M. McDonald, E. D. Bloch, Z. R. Herm, T.-H. Bae and J. R. Long, *Chem. Rev.*, 2012, **112**, 724–781.
13 M. Ding, R. W. Flaig, H.-L. Jiang and O. M. Yaghi, *Chem. Soc. Rev.*, 2019, **48**, 2783–2828.
14 J. Yu, L.-H. Xie, J.-R. Li, Y. Ma, J. M. Seminario and P. B. Balbuena, *Chem. Rev.*, 2017, **117**, 9674–9754.
15 K. S. Song, P. W. Fritz and A. Coskun, *Chem. Soc. Rev.*, 2022, **51**, 9831–9852.
16 P. Bhanja, A. Modak and A. Bhaumik, *ChemCatChem*, 2019, **11**, 244–257.
17 M. G. Mohamed, A. F. M. EL-Mahdy, M. G. Kotp and S.-W. Kuo, *Mater. Adv.*, 2022, **3**, 707–733.
18 D. Liu, W. Gu, L. Zhou, L. Wang, J. Zhang, Y. Liu and J. Lei, *Chem. Eng. J.*, 2022, **427**, 131503.
19 F. Raganati, F. Miccio and P. Ammendola, *Energy Fuels*, 2021, **35**, 12845–12868.
20 W. Xie, D. Cui, S.-R. Zhang, Y.-H. Xu and D.-L. Jiang, *Mater. Horiz.*, 2019, **6**, 1571–1595.
21 B. Gui, X. Liu, Y. Cheng, Y. Zhang, P. Chen, M. He, J. Sun and C. Wang, *Angew. Chem., Int. Ed.*, 2022, **61**, e202113852.
22 M. Perovic, Q. Qin and M. Oschatz, *Adv. Funct. Mater.*, 2020, **30**, 1908371.
23 Y. Zhu, H. Long and W. Zhang, *Chem. Mater.*, 2013, **25**, 1630–1635.
24 M. G. Rabbani and H. M. El-Kaderi, *Chem. Mater.*, 2012, **24**, 1511–1517.
25 S. Gu, J. Guo, Q. Huang, J. He, Y. Fu, G. Kuang, C. Pan and G. Yu, *Macromolecules*, 2017, **50**, 8512–8520.
26 C. Gu, D. Liu, W. Huang, J. Liu and R. Yang, *Polym. Chem.*, 2015, **6**, 7410–7417.
27 H. A. Patel, S. H. Je, J. Park, Y. Jung, A. Coskun and C. T. Yavuz, *Chem.–Eur. J.*, 2014, **20**, 772–780.
28 W. Wang, M. Zhou and D. Yuan, *J. Mater. Chem. A*, 2017, **5**, 1334–1347.
29 H. A. Patel, S. Hyun Je, J. Park, D. P. Chen, Y. Jung, C. T. Yavuz and A. Coskun, *Nat. Commun.*, 2013, **4**, 1357.
30 S. Nandi, U. Werner-Zwanziger and R. Vaidhyanathan, *J. Mater. Chem. A*, 2015, **3**, 21116–21122.
31 X. Zhu, S. M. Mahurin, S.-H. An, C.-L. Do-Thanh, C. Tian, Y. Li, L. W. Gill, E. W. Hagaman, Z. Bian, J.-H. Zhou, J. Hu, H. Liu and S. Dai, *Chem. Commun.*, 2014, **50**, 7933.
32 J. Lu and J. Zhang, *J. Mater. Chem. A*, 2014, **2**, 13831–13834.
33 J.-X. Zhou, X.-S. Luo, X. Liu, Y. Qiao, P. Wang, D. Mecerreyes, N. Bogliotti, S.-L. Chen and M.-H. Huang, *J. Mater. Chem. A*, 2018, **6**, 5608–5612.
34 P. Arab, M. G. Rabbani, A. K. Sekizkardes, T. İslamoğlu and H. M. El-Kaderi, *Chem. Mater.*, 2014, **26**, 1385–1392.
35 P. Arab, E. Parrish, T. İslamoğlu and H. M. El-Kaderi, *J. Mater. Chem. A*, 2015, **3**, 20586–20594.
36 A. Modak, M. Nandi, J. Mondal and A. Bhaumik, *Chem. Commun.*, 2012, **48**, 248–250.
37 L. Feng, K.-Y. Wang, E. Joseph and H.-C. Zhou, *Trends Chem.*, 2020, **2**, 555–568.

38 W. Ji, T.-X. Wang, X. Ding, S. Lei and B.-H. Han, *Coord. Chem. Rev.*, 2021, **439**, 213875.
39 L. Jin, S. Lv, Y. Miao, D. Liu and F. Song, *ChemCatChem*, 2021, **13**, 140–152.
40 Y. Zhu, D. Zhu, Y. Chen, Q. Yan, C.-Y. Liu, K. Ling, Y. Liu, D. Lee, X. Wu, T. P. Senftle and R. Verduzco, *Chem. Sci.*, 2021, **12**, 16092–16099.
41 Y. Xu, Z. Li, F. Zhang, X. Zhuang, Z. Zeng and J. Wei, *RSC Adv.*, 2016, **6**, 30048–30055.
42 R. Bera, M. Ansari, A. Alam and N. Das, *J. CO_2 Util.*, 2018, **28**, 385–392.
43 X. Jiang, Y. Liu, J. Liu, Y. Luo and Y. Lyu, *RSC Adv.*, 2015, **5**, 98508–98513.
44 L. Tao, F. Niu, D. Zhang, J. Liu, T. Wang and Q. Wang, *RSC Adv.*, 2015, **5**, 96871–96878.
45 K. Youm, Y. Choi, H. Byun, S. Kumar, Y. Cho, N. Hsan and J. Koh, *J. CO_2 Util.*, 2024, **84**, 102854.
46 P. Šutalo, M. Pisačić, I. Biljan and I. Kodrin, *CrystEngComm*, 2022, **24**, 4748–4763.
47 B. Panić, T. Frey, M. Borovina, K. Konopka, M. Sambolec, I. Kodrin and I. Biljan, *Polymers*, 2023, **15**, 229.
48 T. Frey, B. Panić, P. Šutalo, M. Borovina, I. Biljan and I. Kodrin, *CrystEngComm*, 2023, **25**, 3870–3884.
49 N. Cindro, Ž. Car, V. Petrović Peroković, M. Borovina, B. Panić, I. Kodrin and I. Biljan, *Heliyon*, 2023, **9**, e21781.
50 Ž. Car, M. Borovina, B. Panić and I. Biljan, *RSC Adv.*, 2025, **15**, 7332–7339.
51 Y. Hou, E. Zhang, J. Gao, S. Zhang, P. Liu, J.-C. Wang, Y. Zhang, C.-X. Cui and J. Jiang, *Dalton Trans.*, 2020, **49**, 7592–7597.
52 F. M. Wisser, K. Eckhardt, D. Wisser, W. Böhlmann, J. Grothe, E. Brunner and S. Kaskel, *Macromolecules*, 2014, **47**, 4210–4216.
53 Y. Xu, D. Chang, S. Feng, C. Zhang and J.-X. Jiang, *New J. Chem.*, 2016, **40**, 9415–9423.
54 N. R. Kumar, P. Das, A. R. Agrawal, S. K. Mandal and S. S. Zade, *Mater. Adv.*, 2021, **2**, 7473–7481.
55 M. M. Abdelnaby, T. A. Saleh, M. Zeama, M. A. Abdalla, H. M. Ahmed and M. A. Habib, *ACS Omega*, 2022, **7**, 14535–14543.
56 R. Bera, M. Ansari, A. Alam and N. Das, *ACS Appl. Polym. Mater.*, 2019, **1**, 959–968.
57 R. Dawson, E. Stöckel, J. R. Holst, D. J. Adams and A. I. Cooper, *Energy Environ. Sci.*, 2011, **4**, 4239.
58 T. Banerjee, F. Haase, S. Trenker, B. P. Biswal, G. Savasci, V. Duppel, I. Moudrakovski, C. Ochsenfeld and B. V. Lotsch, *Nat. Commun.*, 2019, **10**, 2689.
59 B. Zhang, H. Mao, R. Matheu, J. A. Reimer, S. A. Alshmimri, S. Alshihri and O. M. Yaghi, *J. Am. Chem. Soc.*, 2019, **141**, 11420–11424.
60 H. L. Nguyen, N. Hanikel, S. J. Lyle, C. Zhu, D. M. Proserpio and O. M. Yaghi, *J. Am. Chem. Soc.*, 2020, **142**, 2218–2221.
61 H. L. Nguyen, C. Gropp, Y. Ma, C. Zhu and O. M. Yaghi, *J. Am. Chem. Soc.*, 2020, **142**, 20335–20339.
62 D. Zhu, Y. Zhu, Y. Chen, Q. Yan, H. Wu, C.-Y. Liu, X. Wang, L. B. Alemany, G. Gao, T. P. Senftle, Y. Peng, X. Wu and R. Verduzco, *Nat. Commun.*, 2023, **14**, 2865.
63 M. Yuasa, K. Oyaizu, A. Yamaguchi and M. Kuwakado, *J. Am. Chem. Soc.*, 2004, **126**, 11128–11129.
64 M. Lv, X. Ren, R. Cao, Z. Chang, X. Chang, F. Bai and Y. Li, *Polymers*, 2022, **14**, 4893.
65 W. Chen, W. Yan, S. Wu, Z. Xu, K. W. K. Yeung and C. Yi, *Macromol. Chem. Phys.*, 2010, **211**, 1803–1813.
66 D. O. Ojwang, J. Grins and G. Svensson, *Microporous Mesoporous Mater.*, 2018, **272**, 70–78.
67 B. Nath, W.-H. Li, J.-H. Huang, G.-E. Wang, Z. Fu, M.-S. Yao and G. Xu, *CrystEngComm*, 2016, **18**, 4259–4263.
68 H. Liao, H. Wang, H. Ding, X. Meng, H. Xu, B. Wang, X. Ai and C. Wang, *J. Mater. Chem. A*, 2016, **4**, 7416–7421.
69 A. L. Spek, *Acta Crystallogr., Sect. D: Biol. Crystallogr.*, 2009, **65**, 148–155.
70 K. Momma and F. Izumi, *J. Appl. Crystallogr.*, 2011, **44**, 1272–1276.
71 R. Dovesi, A. Erba, R. Orlando, C. M. Zicovich-Wilson, B. Civalleri, L. Maschio, M. Rérat, S. Casassa, J. Baima, S. Salustro and B. Kirtman, *WIREs Comput. Mol. Sci.*, 2018, **8**, e1360.
72 J. P. Perdew, J. A. Chevary, S. H. Vosko, K. A. Jackson, M. R. Pederson, D. J. Singh and C. Fiolhais, *Phys. Rev. B: Condens. Matter Mater. Phys.*, 1992, **46**, 6671–6687.
73 S. Grimme, J. Antony, S. Ehrlich and H. Krieg, *J. Chem. Phys.*, 2010, **132**, 154104.
74 D. Vilela Oliveira, J. Laun, M. F. Peintinger and T. Bredow, *J. Comput. Chem.*, 2019, **40**, 2364–2376.
75 T. Björkman, *Comput. Phys. Commun.*, 2011, **182**, 1183–1186.
76 C. Campañá, B. Mussard and T. K. Woo, *J. Chem. Theory Comput.*, 2009, **5**, 2866–2878.
77 T. F. Willems, C. H. Rycroft, M. Kazi, J. C. Meza and M. Haranczyk, *Microporous Mesoporous Mater.*, 2012, **149**, 134–141.
78 D. Dubbeldam, S. Calero, D. E. Ellis and R. Q. Snurr, *Mol. Simul.*, 2016, **42**, 81–101.
79 M. G. Martin and J. I. Siepmann, *J. Phys. Chem. B*, 1998, **102**, 2569–2577.
80 S. L. Mayo, B. D. Olafson and W. A. Goddard, *J. Phys. Chem.*, 1990, **94**, 8897–8909.